Particles II
Access the latest eBook →

Impact on Biological Systems and the Environment

This eBook is dedicated to the research of Professor David Wertheim. In collaboration with various groups, Professor Wertheim uses confocal microscopy to analyse the impact of different types of particles on human health and the environment, with a focus on human health-hazardous particles detected with solid-state nuclear track detectors (SSNTD). Download for free, today.

11
Advanced Optical Metrology
Particles II

EVIDENT
OLYMPUS

WILEY

Resolving the Role of Configurational Entropy in Improving Cycling Performance of Multicomponent Hexacyanoferrate Cathodes for Sodium-Ion Batteries

Yanjiao Ma, Yang Hu, Yohanes Pramudya, Thomas Diemant, Qingsong Wang, Damian Goonetilleke, Yushu Tang, Bei Zhou, Horst Hahn, Wolfgang Wenzel, Maximilian Fichtner, Yuan Ma,* Ben Breitung,* and Torsten Brezesinski*

Mn-based hexacyanoferrate (Mn-HCF) cathodes for Na-ion batteries usually suffer from poor reversibility and capacity decay resulting from unfavorable phase transitions and structural degradation during cycling. To address this issue, the high-entropy concept is here applied to Mn-HCF materials, significantly improving the sodium storage capabilities of this system via a solid-solution mechanism with minor crystallographic changes upon de-/sodiation. Complementary structural, electrochemical, and computational characterization methods are used to compare the behavior of high-, medium-, and low-entropy multicomponent Mn-HCFs resolving, to our knowledge for the first time, the link between configurational entropy/compositional disorder (entropy-mediated suppression of phase transitions, etc.) and cycling performance/stability in this promising class of next-generation cathode materials.

1. Introduction

The high-entropy concept has been applied recently to various functional materials and has proven beneficial for the structural stability as well as energy storage and conversion efficiency.[1–7]

Y. Ma, Y. Pramudya, Q. Wang, D. Goonetilleke, Y. Tang, B. Zhou,
H. Hahn, W. Wenzel, M. Fichtner, Y. Ma, B. Breitung, T. Brezesinski
Institute of Nanotechnology
Karlsruhe Institute of Technology (KIT)
Hermann-von-Helmholtz Platz 1 76344, Eggenstein-Leopoldshafen,
Germany
E-mail: yuan.ma@kit.edu; ben.breitung@kit.edu;
torsten.brezesinski@kit.edu
Y. Hu, T. Diemant, H. Hahn, M. Fichtner
Helmholtz Institute Ulm (HIU) for Electrochemical Energy Storage
Helmholtzstr. 11 89081, Ulm, Germany
H. Hahn
Joint Research Laboratory Nanomaterials – Technische Universität
Darmstadt and Karlsruhe Institute of Technology (KIT)
Otto-Berndt-Str. 3 64206, Darmstadt, Germany

For multicomponent materials, high configurational entropy is usually achieved by introducing large numbers of different elements into a single-phase structure, leading to many possible combinations of interactions. In the field of electrochemical energy storage, recent reports have shown that increasing configurational entropy (compositional disorder) can have a positive effect on the battery performance and stability.[8–15] Most research has been conducted on oxides and oxyfluorides with rock-salt[10,13,14,16,17] and layered structures,[15,18] where entropy stabilization of the host matrix affects their properties. In our latest report, we have successfully introduced the high-entropy concept into metal-organic frameworks (MOFs) to produce a robust Prussian blue analogue (PBA) cathode for reversible sodium insertion/extraction.[19] Although the multicomponent material showed improved cycling stability compared with conventional unary and binary PBAs, the high-entropy concept needs to be further explored to better understand the mechanism of action in this materials system and its effect on battery performance.

Among the existing PBAs, manganese-based hexacyanoferrates ($Na_xMn[Fe(CN)_6]$, referred to as Mn-HCFs) have been reported as being the most promising cathode materials for sodium-ion battery (SIB) applications (owing to high abundance, sustainability, low costs, high average voltage, among others).[20–22] However, Mn-HCFs suffer from more severe phase transitions than other PBAs caused by cooperative Jahn–Teller distortion of the $Mn-N_6$ octahedra, leading to poor reversibility and fast capacity decay during cycling.[20,23,24] Previous efforts to partially substitute Mn for other redox-active metal species were aimed at mitigating structural distortion and improving the sodium storage properties.[22,25] However, the effect of individual cation doping has generally been considered without addressing the effect of compositional disorder.

Herein, the high-entropy concept is applied to Mn-HCFs. Four metal ions (Fe, Co, Ni, and Cu) were incorporated to produce a high-entropy Mn-based HCF material having the chemical formula $Na_xMn_{0.4}Fe_{0.15}Ni_{0.15}Cu_{0.15}Co_{0.15}[Fe(CN)_6]$ (HEM-HCF, 40% Mn). This sample shows significant improvements in sodium storage compared with medium-entropy HCF

**ADVANCED
SCIENCE NEWS**

www.advancedsciencenews.com

**ADVANCED
FUNCTIONAL
MATERIALS**

www.afm-journal.de
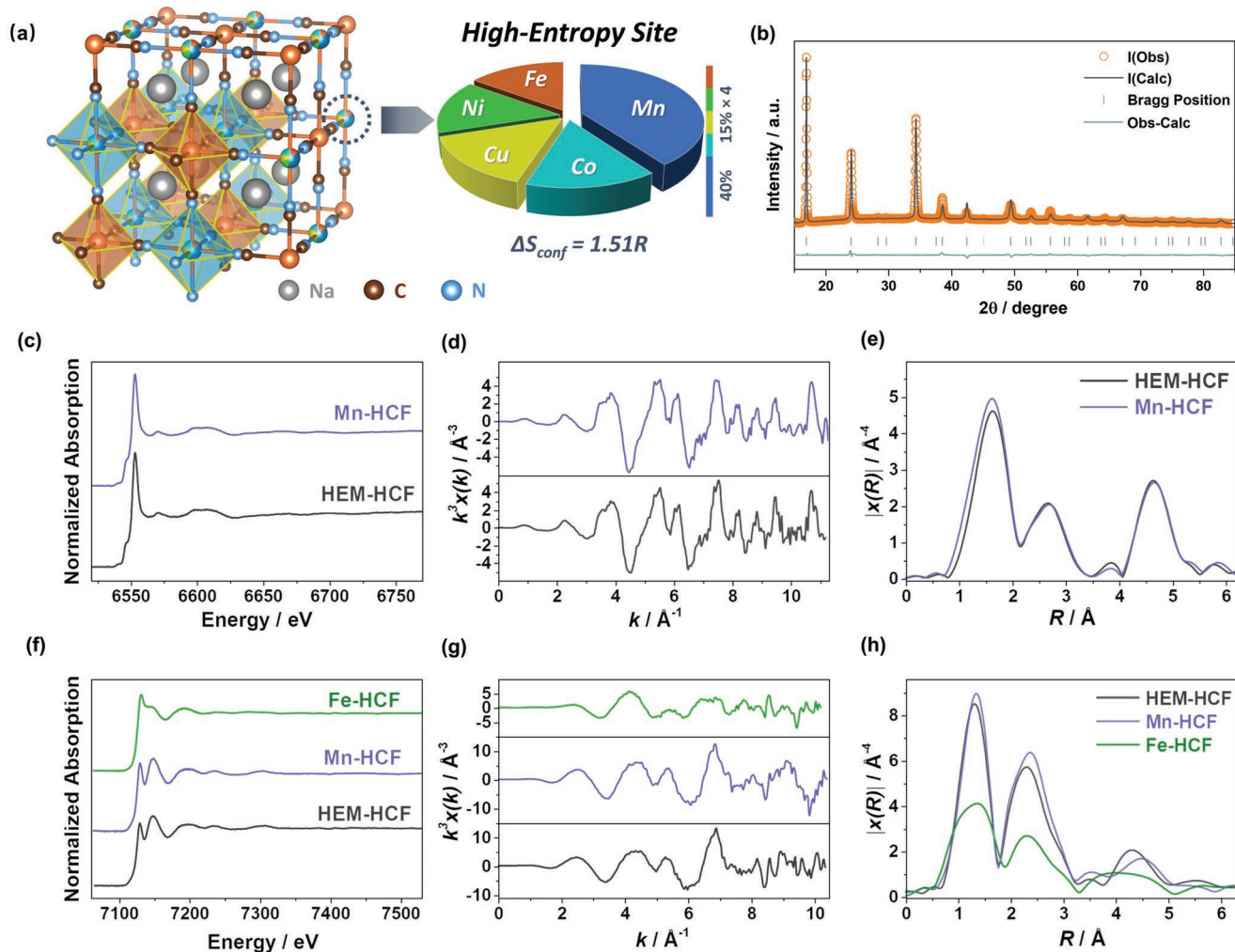
Figure 1. a) Schematic illustration of the crystal structure of HEM-HCF. b) XRD pattern collected from HEM-HCF and corresponding Rietveld refinement profile. c–e) Comparison of XAS data from HEM- and Mn-HCF. c) Normalized Mn K-edge spectra (stacked), d) k^3-weighted $\chi(k)$ spectra, and e) Fourier transforms of the k^3-weighted $\chi(k)$ spectra. f–h) Comparison of XAS data from HEM-, Mn-, and Fe-HCF. f) Normalized Fe K-edge spectra (stacked), g) k^3-weighted $\chi(k)$ spectra, and h) Fourier transforms of the k^3-weighted $\chi(k)$ spectra. Note that a Hanning window function with width $dk = 2$ was applied.

(MEM-HCF, 60% Mn), low-entropy HCF (LEM-HCF, 80% Mn) and conventional (single-metal) Mn-based HCF (Mn-HCF, 100% Mn). Using a suite of complementary characterization techniques, including electron microscopy, operando X-ray diffraction (XRD), X-ray absorption spectroscopy (XAS), X-ray emission spectroscopy (XES), and X-ray photoelectron spectroscopy (XPS), with density functional theory (DFT) calculations, we unveil the role of configurational entropy in the cycling performance of Mn-HCF SIB cathodes and provide a knowledge link between multicomponent materials and their electrochemical behavior.

2. Results and Discussion

The structure of the HEM-HCF sample is depicted in **Figure 1**a. The Fe$_2$, Mn, Co, Ni, and Cu atoms share the same nitrogen-coordinated (M) position in the PBA lattice (Na$_x$M[Fe(CN)$_6$]),

with Mn occupying the majority of this site. Using the definition derived from statistical thermodynamics, see Equations S1 and S2, Supporting Information, the configurational entropy (ΔS_{conf}) was calculated to be 1.51 R. MEM- and LEM-HCFs with a lower ΔS_{conf} of 1.23 R and 0.78 R, respectively, were also prepared. The composition of the different materials employed in this work, from inductively coupled plasma-optical emission spectroscopy (ICP-OES) and thermogravimetric analysis (TGA, see Figure S1, Supporting Information), is shown in Table S1, Supporting Information. For HEM-HCF, the chemical formula was determined to be Na$_{1.26}$Mn$_{0.4}$Fe$_{0.15}$Ni$_{0.15}$Cu$_{0.15}$Co$_{0.15}$[Fe(CN)$_6$]$_{0.81}$□$_{0.19}$·1.12H$_2$O.

The XRD patterns shown in Figure 1b and Figure S1, Supporting Information, indicate that the samples adopt a cubic crystal symmetry and further suggest that they are free of impurity phases. A structural model with space group Fm-$3m$ (ICSD coll. code 193 353)[26] was refined against data collected from the HEM-HCF sample. The corresponding Rietveld refinement

2202372 (2 of 11)

ADVANCED
SCIENCE NEWS

www.advancedsciencenews.com

ADVANCED
FUNCTIONAL
MATERIALS

www.afm-journal.de
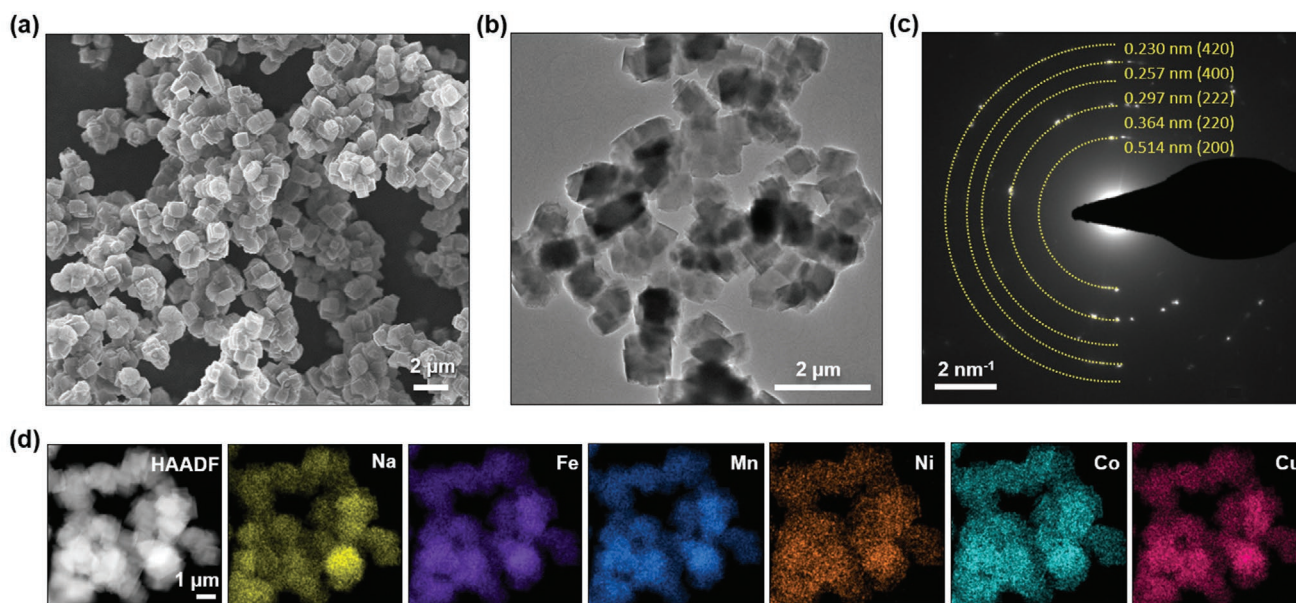
Figure 2. a) SEM image, b) TEM image, c) SAED pattern, and d) HAADF STEM image and corresponding EDS elemental maps for HEM-HCF.

profile and structural parameters are shown in Figure 1b and Table S2, Supporting Information, respectively. The structural model assumes that the carbon-coordinated Fe$_1$ atoms occupy the 4a site (Wyckoff position), while the nitrogen-coordinated Fe$_2$, Mn, Co, Ni, and Cu atoms share the 4b site (Figure 1a). It suggests that the structure consists of linear chains of −Fe$_1$−C≡N−Mn/Co/Ni/Cu/Fe$_2$−N≡C−Fe$_1$− along the unit-cell axes. The lattice parameter of HEM-HCF was determined to be $a = 10.4067(7)$ Å, a slight decrease compared to the conventional Mn-HCF for which $a = 10.4275(7)$ Å (see Table S3, Supporting Information).

XAS was conducted to probe the oxidation state and local environment of the different metal ions. K-edge extended X-ray absorption fine structure (EXAFS) spectra and corresponding Fourier transforms of the k^3-weighted $\chi(k)$ spectra are shown for the HEM-HCF sample in Figure S2, Supporting Information. Figure 1c–e compares the Mn K-edge data from HEM- and Mn-HCF. Very similar radial distribution of half-path lengths were obtained, showing three distinct features corresponding to the M−N, M−C, and M−M shells.[27,28] This result suggests that the 4b (M) site (Fe$_2$, Mn, Co, Ni, and Cu) in HEM-HCF has the same coordination environment as the Mn site in Mn-HCF, namely −Fe(4a)−C≡N−M(4b)−N≡C−Fe(4a)−. Fe K-edge data collected from the HEM-, Mn-, and Fe-HCF materials (Figure 1f–h) again showed that the radial distribution of half-path lengths is similar for the Mn-based HCFs, due to the dominating contribution of −Fe(4a)−C≡N− and zero (for Mn-HCF) or minor contribution (for HEM-HCF) of −Fe(4b)−N≡C−. In contrast, a distinct distribution of the first shell was observed for Fe-HCF as a combination of Fe contributions in the −Fe(4a)−C≡N− and −Fe(4b)−N≡C− coordinations (with distinguishable metal-ligand spacings).

Scanning electron microscopy (SEM) and transmission electron microscopy (TEM), see **Figure 2**a and 2b, respectively, showed that the HEM-HCF particles are cubic in shape and have an average size of 1 µm. Reflections corresponding to the

(200), (220), (222), (400), and (420) lattice planes are clearly visible in the selected-area electron diffraction (SAED) pattern in Figure 2c. In addition, high-angle annular dark-field scanning TEM (HAADF STEM) imaging and energy dispersive X-ray spectroscopy (EDS) mapping confirmed the uniform distribution of Na, Fe, Mn, Co, Ni, and Cu at the given resolution (Figure 2d). Both MEM- and LEM-HCF were found to have a similar morphology and particle size, as shown in Figure S3, Supporting Information.

XPS was used to characterize the surface composition of the HEM-HCF sample. The measurement also confirmed the presence of the different elements (**Figure 3**a–f). The Na 1s detail spectrum showed a single peak at a binding energy of 1071.8 eV.[29] The spectrum of the Fe 2p core-level region revealed peaks at 708.4 (2p$_{3/2}$) and 721.2 eV (2p$_{1/2}$), similar to the binding energies reported by Sarhid et al.[30] for K$_4$[Fe(CN)$_6$]. In contrast, the Fe 2p$_{3/2}$ and 2p$_{1/2}$ peaks for K$_3$[Fe(CN)$_6$] appeared at ≈710 and ≈723 eV, respectively. Note that the nitrogen-coordinated Fe$_2$ ions also contribute to the peak structure, and it can be assumed that they are in +2 oxidation state, too.[19,31] Analysis of the Mn 2p data is complicated by the presence of a Ni Auger line at 644 eV. The major Mn 2p peaks were detected at 641.4 and 653.1 eV, accompanied by shake-up satellites at 646.0 and 657.7 eV. The binding energy of the Mn 2p$_{3/2}$ peak is characteristic of Mn in oxidation state +2 or +3. Clear differentiation between the two oxidation states is not possible from the binding energy alone. However, the satellite peaks point to the presence of Mn^{2+}.[19,32,33] Similarly, the Co 2p spectrum showed distinct satellite peaks at 789.1 and 804.6 eV, in addition to the main peaks at 781.9 (Co 2p$_{3/2}$) and 797.4 eV (Co 2p$_{1/2}$) and a Fe Auger line at 786 eV. Because satellite structures are usually observed for Co^{2+} only, it can be assumed that Co is present in oxidation state +2.[19,34] The Ni 2p spectrum showed major peaks at 856.2 (Ni 2p$_{3/2}$) and 873.8 eV (Ni 2p$_{1/2}$) together with a doublet at slightly higher binding energies of 857.4 and 874.9 eV and satellite peaks at 862.7 and 880.1 eV. Note that oxidized Ni

**ADVANCED
SCIENCE NEWS**

www.advancedsciencenews.com

**ADVANCED
FUNCTIONAL
MATERIALS**

www.afm-journal.de
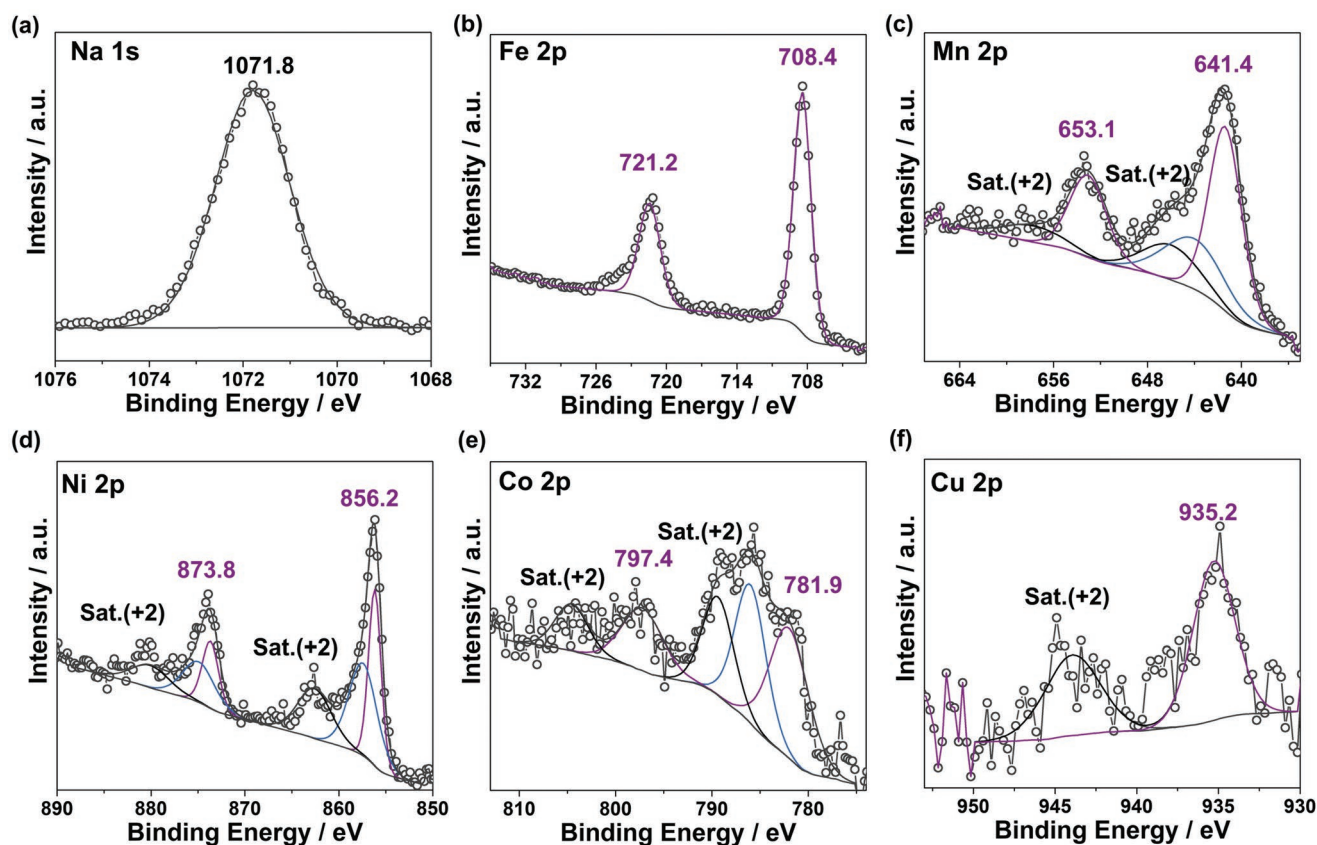
Figure 3. XPS detail spectra of the a) Na 1s, b) Fe 2p, c) Mn 2p, d) Ni 2p, e) Co 2p, and f) Cu 2p regions for HEM-HCF.

species have been shown to lead to rather complex multiplet splittings.[35] This means it is not necessarily an indication of mixed oxidation states. Furthermore, the Ni $2p_{3/2}$ binding energy is not well suited to discriminate between Ni^{2+} and Ni^{3+} species. For instance, while the Ni $2p_{3/2}$ peak of NiO is centered around 854 eV, it was found at ≈856 eV for $Ni(OH)_2$, a similar binding energy to that of Ni_2O_3. Finally, from the binding energy of the Cu $2p_{3/2}$ peak (935.2 eV) and the presence of a shake-up satellite (944 eV), +2 oxidation state can be assigned to the Cu.[19,36] Similar XPS results were obtained for both MEM- and LEM-HCF, see Figure S4, Supporting Information.

Figure 4a–e shows normalized K-edge X-ray absorption near edge spectroscopy (XANES) data collected from the same HCF samples and various reference materials. The average oxidation states were determined by "fingerprint" comparisons with known standards, most of which are metal oxides with octahedral coordination environments, corresponding to the M-N_6 and Fe-C_6 units in the HCFs (see Table S4, Supporting Information). The Mn, Co, Ni, and Cu data for HEM-HCF revealed XANES features comparable to reported near-edge structures of conventional HCF materials.[37–41] The Mn, Co, and Cu K-edge spectra showed a distinct edge position close to that of MnO, CoO, and CuO, respectively, as seen in Figure 4b,d, and 4e, indicating a similar formal oxidation state of +2. The energy shifts of the Ni K-edge were much less pronounced (Figure 4c). Therefore, the (energy) positions of the first peak in the first derivative (d$\mu(E)$/dE) were compared, suggesting that the Ni in HEM-HCF has a formal oxidation state between +2

and +3. The Fe K-edge spectra (Figure 4a) for HEM-, Mn-, and Fe-HCF showed an edge position similar to Fe_2O_3, as well as to $K_4[Fe(CN)_6]\cdot3H_2O$ and $K_3[Fe(CN)_6]$, despite the different oxidation state of Fe in these standard reference materials. This is because the absorption at the Fe K-edge is very sensitive to the ligand type, covalency, and Fe spin state.[42] The opposing effects of covalency and changing d-count can lead to subtle changes in the absorption edge. This means little information about the oxidation state of Fe can be obtained by XANES fingerprinting.

XES measurements were thus conducted to gain more insight into the oxidation and spin states of Fe, see Figure 4f. The $K\beta$ emission lines of first-row transition metals correspond to the process of $3p$ electron refilling a $1s$ core hole ($1s^13p^63d^n$), resulting in a $1s^23p^53d^n$ final state. The $3p$–$3d$ exchange coupling leads to line splitting (into $K\beta_{1,3}$ and $K\beta'$), with the relative intensity of the $K\beta'$ feature depending on the number of unpaired $3d$ electrons. Both the HEM- and Mn-HCF samples as well as the $K_4[Fe(CN)_6]\cdot3H_2O$ and $K_3[Fe(CN)_6]$ standard reference materials showed a weak $K\beta'$, indicating a low number of unpaired electrons and evidencing low-spin (LS) electron configuration (i.e., $1s^23p^5t_{2g}{}^ne_g{}^0$). By contrast, Fe-HCF revealed a distinct $K\beta_{1,3}$-$K\beta'$ splitting (with a relatively lower $K\beta'$ intensity). This suggests mixed contribution of LS and high-spin (HS) Fe for the $-Fe-C\equiv N-$ and $-Fe-N\equiv C-$ coordination, respectively. Previous reports have also shown that the $K\beta_{1,3}$ line of Fe-based materials shifts to higher energies with increasing nominal spin value (S), reflecting both oxidation and spin state.[43,44] $K_4[Fe(CN)_6]\cdot3H_2O$ has a well-defined LS Fe^{2+} ($1s^23p^5t_{2g}{}^6e_g{}^0$)

**ADVANCED
SCIENCE NEWS**

www.advancedsciencenews.com

**ADVANCED
FUNCTIONAL
MATERIALS**

www.afm-journal.de
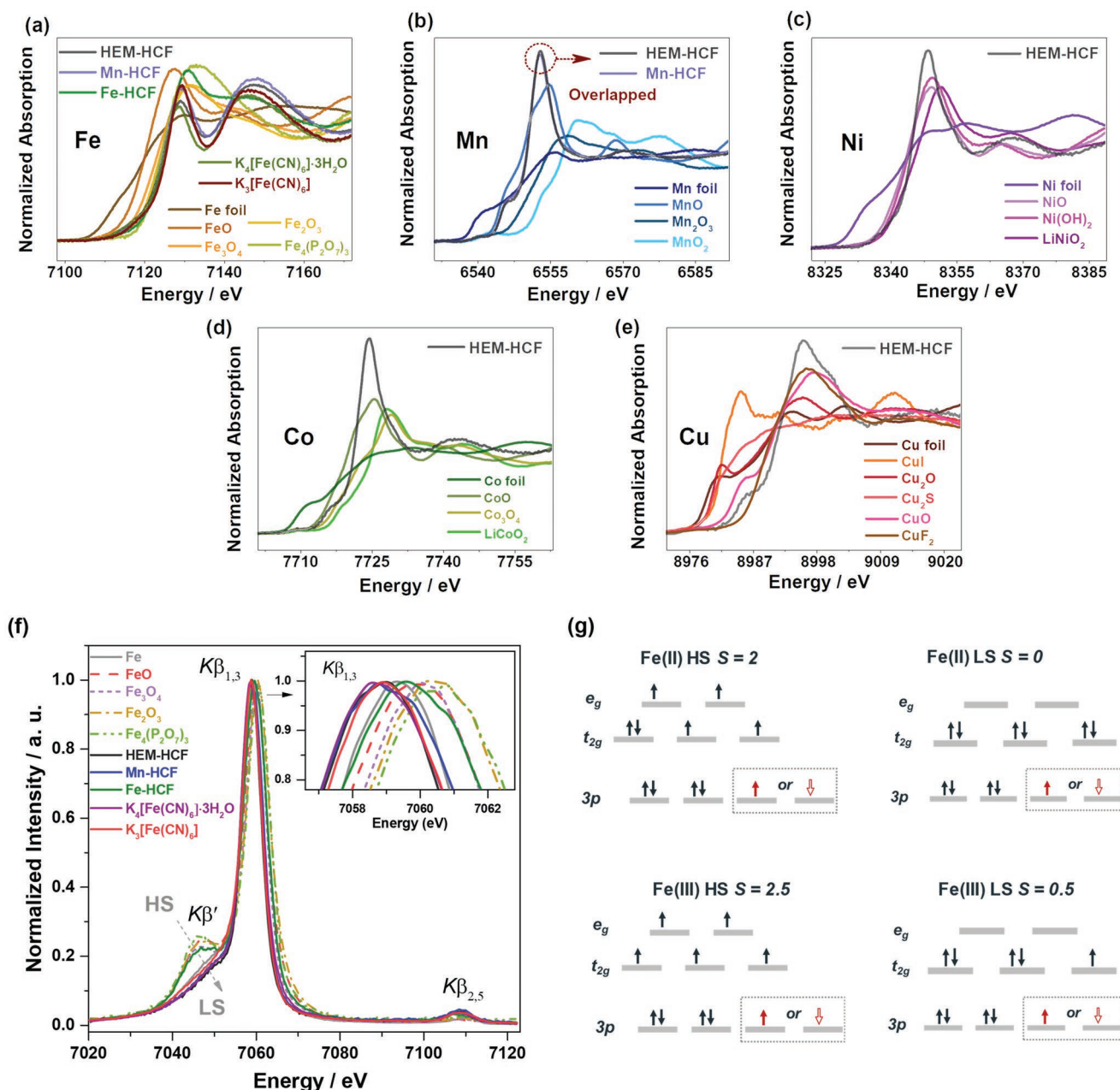
Figure 4. Normalized a) Fe, b) Mn, c) Ni, d) Co, and e) Cu K-edge XANES data and f) Fe $K\beta$ XES of different HCF and standard reference materials. The inset in (f) shows the $K\beta_{1,3}$ lines. Note that the spectra were normalized by peak intensity. g) Simplified depiction of the corresponding excited states of Fe (+2 and +3, HS and LS).

configuration with a nominal spin value $S = 0$, and its $K\beta_{1,3}$ peak was centered at the lowest energy, as expected. The $K\beta_{1,3}$ line for the HS standards tested indeed steadily increased in energy from FeO ($1s^2 3p^5 t_{2g}{}^4 e_g{}^2$, $S = 2$) and Fe_3O_4 ($S = 2.33$) to Fe_2O_3 ($S = 2.5$) and $Fe_4(P_2O_7)_3$ ($1s^2 3p^5 t_{2g}{}^3 e_g{}^2$, $S = 2.5$), in agreement with the literature. HEM- and Mn-HCF showed a similar $K\beta_{1,3}$ line position to that of $K_4[Fe(CN)_6] \cdot 3H_2O$, with the energy being slightly lower than for $K_3[Fe(CN)_6]$ (LS, $1s^2 3p^5 t_{2g}{}^5 e_g{}^0$, $S = 0.5$), thereby indicating that the majority of Fe^{2+} ions (LS, $S = 0$) are coordinated to C ($-Fe-C\equiv N-$). On the other hand, the energy position of the Fe-HCF $K\beta_{1,3}$ line was between

that of Fe metal (LS, $S = 1$) and FeO (HS, $S = 2$), suggesting a $Na_x Fe^{3+}$(HS, $S = 2.5$)$[Fe^{2+}$(LS, $S = 0$)(CN)$_6$] configuration.

From the XPS, XAS, and XES results, the formal oxidation state(s) of the transition metal ions can be derived for the different HCFs (see Table S5, Supporting Information). Overall, the data indicate that the average oxidation state of both the carbon-coordinated Fe_1 and nitrogen-coordinated M (Fe_2, Mn, Co, Ni, and Cu) atoms is +2, as expected for the structure consisting of linear chains of $-Fe^{2+}-C\equiv N-M^{2+}-N\equiv C-Fe^{2+}-$.

Having established the structural and chemical properties of the HCF samples, the impact of these on their electrochemical
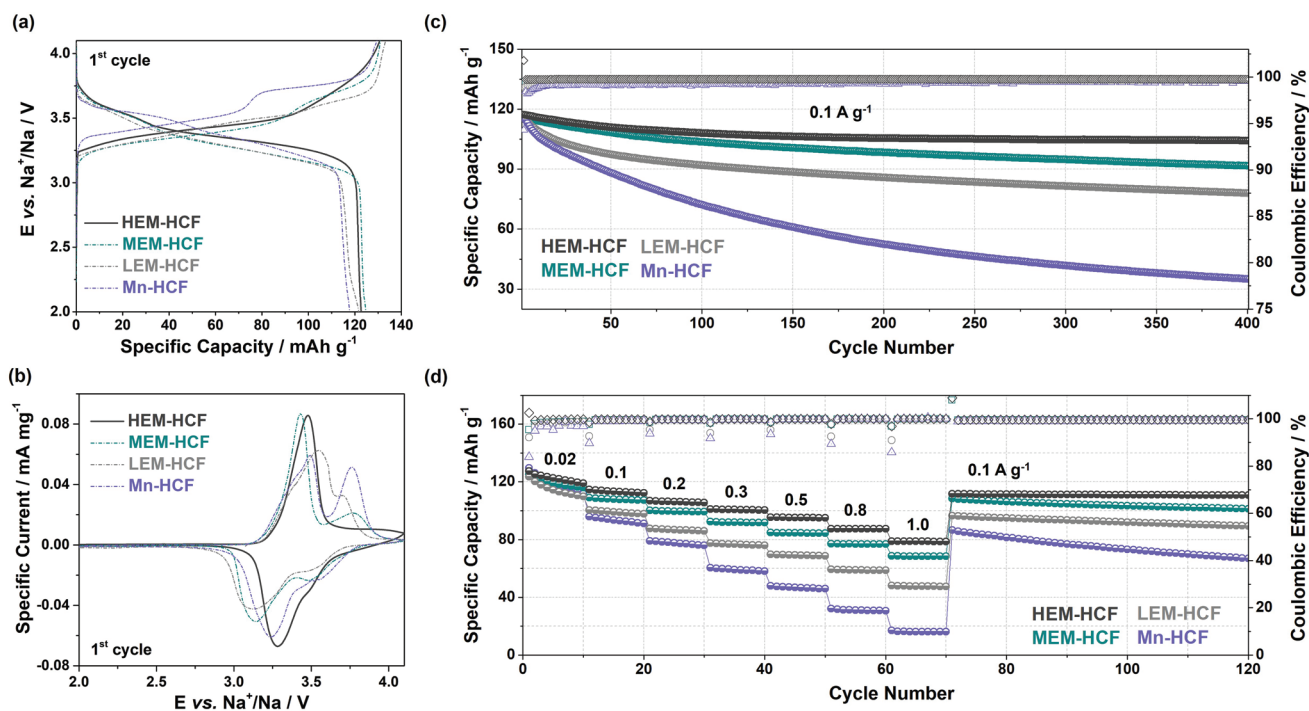
Figure 5. a) First-cycle voltage profiles at 0.01 A g^{-1}, b) cyclic voltammograms at 0.05 mV s^{-1}, c) long-term cycling performance at 0.1 A g^{-1}, and d) rate capability of SIB cells using the HEM-, MEM-, LEM-, and Mn-HCF cathodes. Note that at least three individual cells per sample were tested to ensure reproducibility. The data presented here are those closest to the average. See Figure S5, Supporting Information, for standard deviations.

behavior was investigated. Cathodes prepared from the HEM-, MEM-, LEM-, and Mn-HCF materials were subjected to galvanostatic cycling in SIB cells. All of them delivered a similar first-cycle specific discharge capacity of ≈120 mAh g^{-1} at 0.01 A g^{-1} with a relatively high average voltage (HEM-HCF (3.32 V) ≈ Mn-HCF > MEM-HCF (3.14 V) ≈ LEM-HCF), see **Figure 5**a. Two characteristic plateaus at 3.76/3.53 and 3.49/3.24 V were observed in the voltage profile of Mn-HCF, which is consistent with the cyclic voltammetry (CV) data shown in Figure 5b. They correspond to the nitrogen-coordinated HS Mn$^{2+/3+}$ and carbon-coordinated LS Fe$^{2+/3+}$ redox couple, respectively.[20–22,45] For MEM- and LEM-HCF, the redox features were still apparent but more difficult to distinguish, due to the introduction of multiple metal species into the 4b site. Interestingly, they merged into broad, asymmetric peaks upon further increasing the ΔS_{conf} of the system, as can be seen for HEM-HCF (Figure 5b), accompanied by an increase in average voltage. Varying the configurational entropy of the system also strongly affected the Coulombic efficiency. Mn-HCF and LEM-HCF revealed a lower first-cycle Coulombic efficiency of 90.7%, compared to 94.9% for both HEM- and MEM-HCF. Furthermore, HEM-HCF showed the lowest voltage hysteresis of 0.19 V, significantly lower than that for MEM-HCF (0.29 V), LEM-HCF (0.44 V), and Mn-HCF (0.38 V), highlighting clear benefits to energy efficiency. The superior performance of HEM-HCF was also evident in the subsequent cycles. At a specific current of 0.1 A g^{-1}, it delivered an initial specific capacity of 117 mAh g^{-1}, and the cyclability was much better than for the other HCFs. The capacity retention after 200 cycles was 90% for HEM-HCF, 85% for MEM-HCF, 80% for LEM-HCF, and only 46% for Mn-HCF (Figure 5c), indicating that the degree

of compositional disorder has a profound effect on the cycling stability. The same influence was found on the Coulombic efficiency (e.g., 99.8% for HEM-HCF and 99.6% for MEM-HCF, compared to 99.2% and 98.9% for LEM- and Mn-HCF, respectively, in the 50th cycle). Similarly, HEM-HCF showed improved rate capability (Figure 5d). For instance, at 0.5, 0.8, and 1.0 A g^{-1}, it was still capable of delivering 96, 87, and 79 mAh g^{-1}, respectively. For MEM-, LEM-, and Mn-HCF, the specific capacity at higher rates was significantly reduced, especially for the latter materials. At the highest rate, they only delivered ≈47 and ≈16 mAh g^{-1}, respectively. Upon reducing the specific current back to 0.1 A g^{-1}, the specific capacity of HEM-HCF recovered and stabilized at 112 mAh g^{-1}, emphasizing the improved reversibility of the de-/sodiation reactions. Overall, the high-entropy sample clearly outperformed all other HCFs tested in this work.

To examine the influence of configurational entropy on the de-/sodiation mechanism and better understand the reason for the differences in cycling performance and stability, operando XRD measurements were conducted during battery operation. As can be seen from **Figure 6**a,d, the HEM-HCF sample displayed a solid-solution type behavior,[19,46,47] with subtle peak changes during cycling. In the first charge cycle, the reflections showed a continuous but very small shift to higher 2θ values, due to contraction of the unit cell upon Na$^+$ extraction, along with some peak broadening. In the subsequent sodiation (discharge) cycle, they shifted back toward their initial position. The same behavior was observed in the second cycle, highlighting the overall reversibility. In contrast to conventional HCFs,[23,24,40,48–52] no phase transition occurred throughout the measurement. Figure 6d depicts contour plots of the

**ADVANCED
SCIENCE NEWS**

www.advancedsciencenews.com

**ADVANCED
FUNCTIONAL
MATERIALS**

www.afm-journal.de
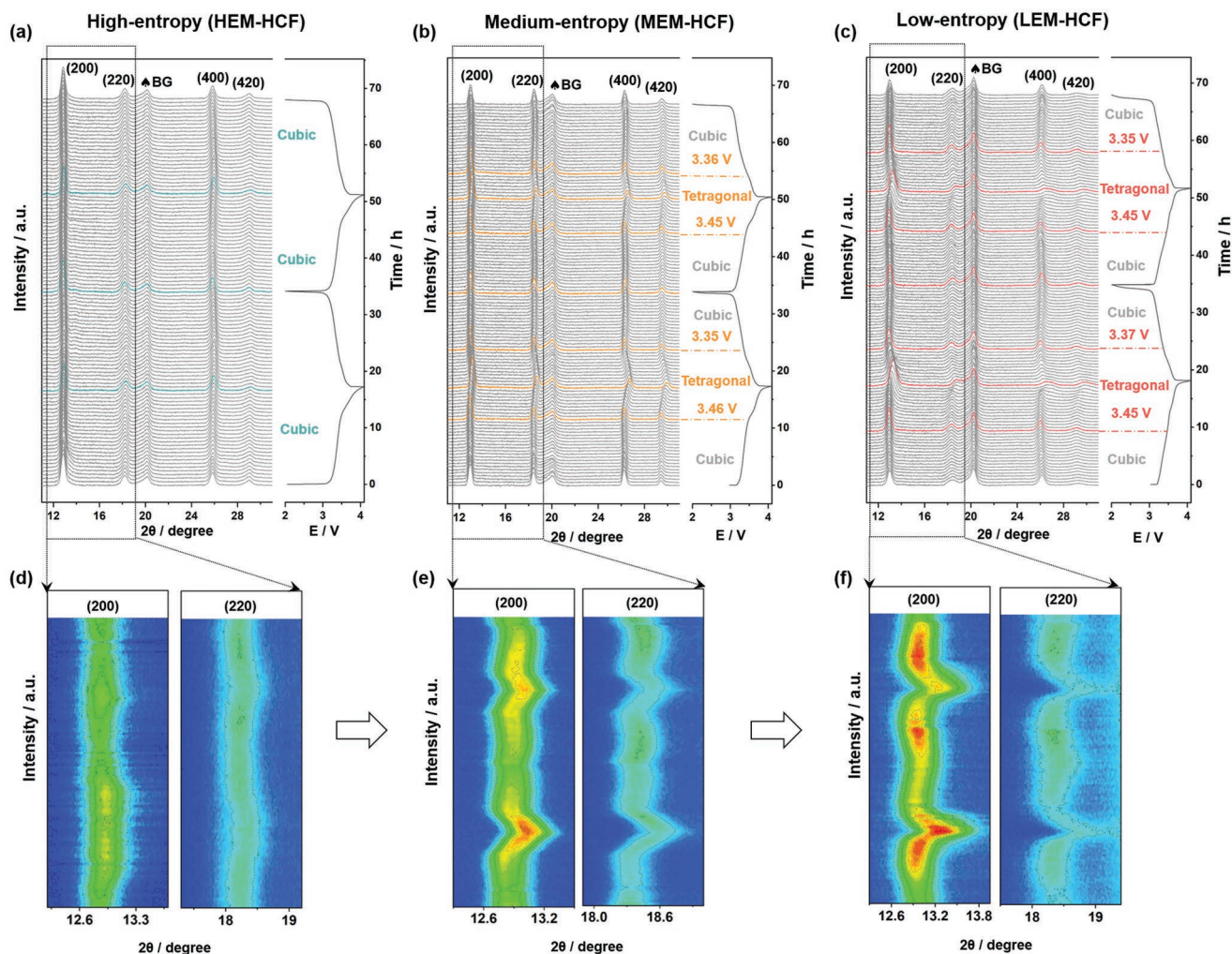
Figure 6. Operando XRD analysis of SIB cells for tracking phase changes during de-/sodiation in the first two cycles. a–c) Waterfall diagrams and corresponding dis-/charge curves as well as d–f) contour plots of XRD patterns for the HEM-, MEM-, and LEM-HCF cathodes.

200 and 220 reflections. The a lattice parameter varied from 10.37 to 10.43 Å, suggesting a nearly zero-strain operation. An operando XRD measurement at the 30th cycle was also performed and is shown in Figure S6, Supporting Information. The structural evolution was found to be quite similar to the initial two cycles, further confirming the high stability and reversibility. Major differences were evident upon reducing the ΔS_{conf} of the system to 1.23 R (medium entropy) and 0.78 R (low entropy). Figure 6b,e shows the operando XRD results for the MEM-HCF cathode. Unlike for the high-entropy material, the structure underwent a phase change from cubic to tetragonal when the cell was charged to 3.46 V, leading to significant volume contraction. Upon subsequent discharge to 3.35 V (sodiation), the tetragonal phase transformed back to the cubic phase. For LEM-HCF (Figure 6c,f), the phase changes were similar but even more pronounced. The transition occurred when the cell reached 3.45 V during charging, and the reflections remained largely unaltered until 3.57 V followed by substantial lattice contraction. Although the structure transformed back with subsequent sodiation, irreversibilities (structural degradation) were already apparent in the second dis-/charge cycle

(e.g., see the 200 reflection in Figure 6f), which agrees with the more rapid capacity fading of LEM-HCF (Figure 5c). For a more detailed comparison, ex-situ XRD patterns were also collected from the pristine and fully sodiated HEM-, MEM-, and LEM-HCF cathodes after 10, 20, and 40 cycles (Figure S7, Supporting Information). As expected, HEM-HCF revealed high reversibility, that is, the cubic structure was well maintained after the 40th cycle. In contrast, for both MEM- and LEM-HCF, some intensity loss and shift of the XRD reflections to higher 2θ values were observed, consistent with the operando XRD data shown in Figure 6.

Overall, the advantage of using a high-entropy material becomes clear by comparing the behavior of the three HCFs. In particular, the increasing (entropy-mediated) suppression of structural degradation and phase transitions in the order of LEM-HCF < MEM-HCF < HEM-HCF provides an explanation for the excellent cycling performance of the latter material. In addition, the results from operando and ex-situ XRD corroborate our conclusion that compositional disorder positively affects the reversibility of the electrochemical reaction with sodium.

**ADVANCED
SCIENCE NEWS**

www.advancedsciencenews.com

**ADVANCED
FUNCTIONAL
MATERIALS**

www.afm-journal.de
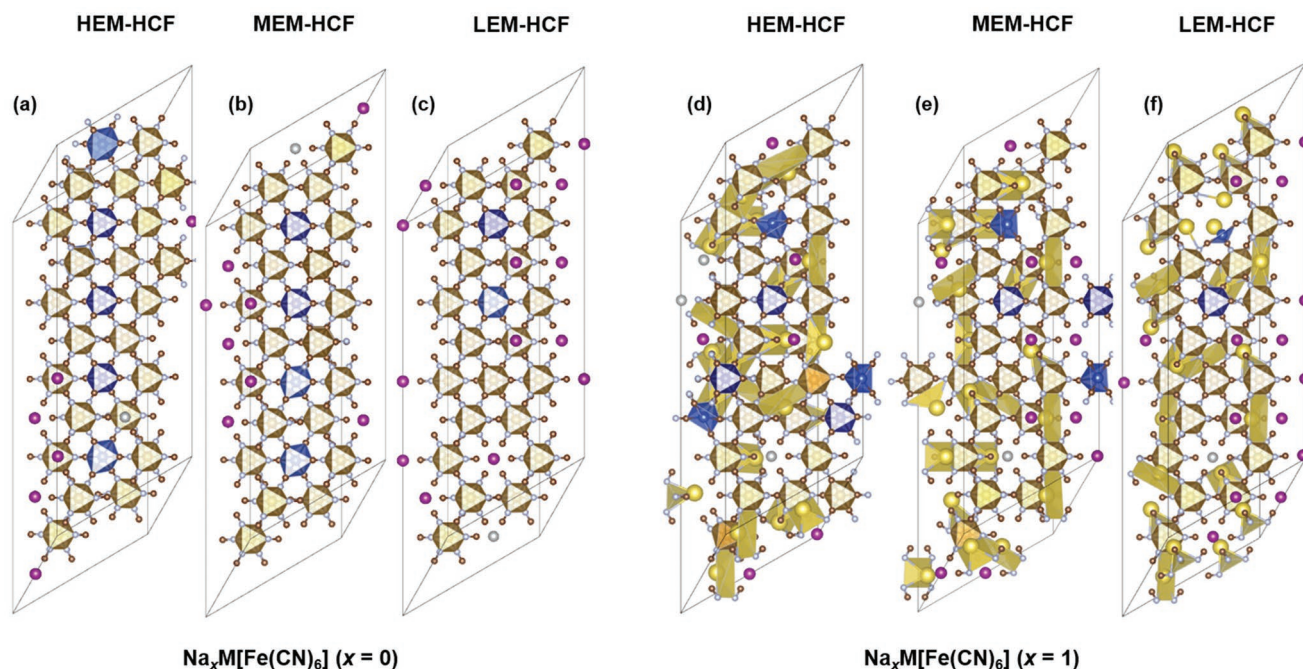
Figure 7. DFT optimized structures for a) HEM-, b) MEM-, and c) LEM-HCF in the fully charged state (i.e., $x = 0$ in $Na_xM[Fe(CN)_6]$). d–f) Corresponding HCF structures for $x = 1$. The C, N, Cu, Co, Ni, Fe, Mn, and Na atoms are shown in brown, bluish gray, blue, dark blue, silver, bronze, purple, and yellow, respectively.

To further advance our understanding of the effect of configurational entropy, DFT calculations were carried out in VASP with PBE functional for the HEM-, MEM-, and LEM-HCF materials. A $2 \times 2 \times 5$ supercell from its primitive cell was used to accommodate the different ratios of Fe, Mn, Co, Ni, and Cu atoms (with initial cubic structure). The results from the calculations are shown in Table S6, Supporting Information. In geometry optimization, the position of the individual atoms is not constrained and there are two setups, namely one with fixed cell parameters (fixed volume) and the other with a fully optimized scheme (allows cell parameters to vary). For $x = 0$ (desodiated state), the formation energy was found to be always the lowest for HEM-HCF, and the entropy gain makes the material even more stable (**Figure 7**a–c). For $x = 1$ (sodiated state), the HEM-HCF sample also had the lowest formation energy (Figure 7d–f). In the fully optimized model, where the cell parameters can vary, MEM-HCF showed a slightly lower formation energy (by 0.01 RT) than HEM-HCF. However, this is still much smaller than the entropic energy gain at temperature T (see Table S1, Supporting Information) for HEM-HCF (1.51 R) relative to MEM-HCF (1.23 R). Overall, the HEM-HCF free energy is lower than that of MEM-HCF by 0.27 RT.

In summary, the DFT results indicate that the HEM-HCF sample has a more robust structure for the de-/sodiation reactions compared to the MEM- and LEM-HCFs, which is consistent with the experimental observations (entropy-mediated suppression of phase transitions, etc.) described above.

Finally, the role of the individual metal species in determining the electrochemical properties of HEM-HCF was investigated. For this purpose, a series of dual-metal MMn-HCFs (M = Ni, Co, Fe, and Cu) having 40% Mn (same Mn content as for HEM-HCF) and 60% M were prepared. A comparison of cyclic voltammograms for the HEM-, NiMn-, CoMn-, FeMn-, and CuMn-HCF cathodes is shown in Figure S8, Supporting Information. NiMn-HCF exhibited a similar electrochemical behavior to HEM-HCF, which is in agreement with our previous study, indicating that the Ni in multicomponent PBAs is electrochemically inactive.[19] On the contrary, all other HCFs showed quite different features. For instance, in addition to the main redox couple at 3.48/3.29 V, another pair of well-defined and rather symmetric peaks appeared at 3.07/2.91 V for FeMn-HCF and at 3.86/3.78 V for CoMn-HCF, corresponding to the HS $Fe^{2+/3+}$ and $Co^{2+/3+}$ redox couple, respectively.[53,54] In the case of CuMn-HCF, both the shift of the main cathodic peak to lower voltages and the asymmetric peak broadening suggest the merging of LS $Fe^{2+/3+}$, HS $Mn^{2+/3+}$, and HS $Cu^{1+/2+}$ redox couples.[19,55] Compared to the dual-metal MMn-HCFs, the HEM-HCF cathode had the highest average voltage and smallest voltage gap between charge and discharge. As can be seen from the voltage profiles in Figure S8, Supporting Information, the CoMn- and FeMn-HCF cathodes delivered first-cycle specific discharge capacities of ≈128 mAh g^{-1}, slightly larger than for HEM-HCF (122 mAh g^{-1}) and CuMn-HCF (120 mAh g^{-1}) but much larger than for NiMn-HCF (99 mAh g^{-1}), corroborating that the Ni is indeed inactive.

Based on these results, we conclude that $Fe^{2+/3+}$, $Mn^{2+/3+}$, $Co^{2+/3+}$, and $Cu^{1+/2+}$ are the main redox-active centers in HEM-HCF, which agrees well with our previous findings.[19] Despite being redox inactive, the presence of Ni is beneficial to the cycling stability, see Figure S8, Supporting Information. NiMn-HCF showed the best capacity retention among the dual-metal Mn-HCFs tested. Similar observations have been made for conventional Ni-based HCFs.[51,56,57]

**ADVANCED
SCIENCE NEWS**

www.advancedsciencenews.com

**ADVANCED
FUNCTIONAL
MATERIALS**

www.afm-journal.de

3. Conclusion

The introduction of high configurational entropy (compositional disorder) into the Mn-HCF has been shown to significantly boost the performance of this system for reversible sodium storage. Systematic comparison of the structural and chemical properties of high-, medium-, and low-entropy Mn-HCFs revealed the origin of the improved performance, via entropy-mediated suppression of phase transitions, among others. Apart from the excellent cyclability, we have established here, to our knowledge for the first time, a link between the high-entropy effect and the observed energy storage capabilities of this promising class of functional materials. It is hoped that these findings could provide a foundation for future investigations into multicomponent HCF cathodes, and also other high-entropy (energy) materials. In particular, the approach seems promising for designing high-quality materials with very low or even without crystal water content to further improve the capacity. This may foster the research and development of multicomponent HCFs for battery applications.

4. Experimental Section

Materials Synthesis: HEM-HCF (40% Mn) was synthesized by a co-precipitation method at room temperature. 8 mmol $Na_4[Fe(CN)_6]$ and 170 mmol NaCl were dissolved in 100 mL deionized water to form solution A. 2 mmol $MnCl_2 \cdot 4H_2O$ and 3 mmol metal precursors ($FeCl_2 \cdot 4H_2O$, $NiCl_2 \cdot 6H_2O$, $CuCl_2 \cdot 2.5H_2O$, and $CoCl_2 \cdot 6H_2O$, 0.75 mmol each) were successively dissolved in 100 mL deionized water to form solution B. Next, 25 mmol sodium citrate was added to solution B, treated via ultrasonication for 0.5 h and then stirred for 1 h. Solutions A and B were slowly and simultaneously dropwise added to 500 mL deionized water under constant magnetic stirring to form solution C. After stirring for 2 h, solution C was aged at room temperature for 24 h. The precipitate was collected by centrifugation, washed several times with deionized water, and dried at 60 °C overnight. The product was carefully ground into a fine powder and further dried at 100 °C in a vacuum oven for 24 h. The MEM-HCF (60% Mn), LEM-HCF (80% Mn), conventional single (Mn-HCF, 100% Mn), and dual metal (MMn-HCF, M = Fe, Co, Cu, and Ni, always 40% Mn) Mn-based hexacyanoferrate samples were prepared analogously by using the respective precursors.

Characterization: The crystal structure of the samples was investigated via powder XRD using either a Bruker D8 Advance (Cu K$_{\alpha1}$ radiation, $\lambda = $ 1.54056 Å), STOE Stadi P diffractometer equipped with a Ga-jet X-ray source (Ga K$_\beta$ radiation, $\lambda = 1.20793$ Å), or STOE Stadi P diffractometer with a Mo anode ($\lambda = 0.70926$ Å) and a DECTRIS MYTHEN 1K strip detector.

Transmission XAS measurements were performed on a laboratory device (easyXAFS300+, easyXAFS LLC), which is based on Rowland circle geometries with spherically bent crystal analyzers (SBCA) and operated using a Mo X-ray tube source and a silicon drift detector (AXAS-M2, KETEK GmbH).[58] Mn, Fe, Co, Ni, and Cu K-edge spectra were collected from dilute powder samples pressed into pellets together with standard reference materials. For the Mn and Fe K-edges, the mass loading of $Na_xM[Fe(CN)_6]$ was calculated based on obtaining a 1 to 1.5 unit-edge step.[59] The Co, Ni, and Cu K-edges were measured using the same sample, which is a compromise between total absorption and signal-to-noise ratio. Both Cu_2S and Cu_2O were stored inside an Ar glovebox, where the pellets were prepared. The pressed pellets were sandwiched by Kapton tape and taken out for XAFS measurements. An energy step of 0.25 eV was used for the XANES region and a step of 0.03 Å^{-1} for the post-edge region. Multiple scans for each sample were performed to improve the signal-to-noise ratio. Metal reference foils (Exafs Materials, Goodfellow) were measured before and after the XAS measurements

of HCF samples and standards for energy calibration, as well as for monitoring the energy drift. More details on the sample preparation and data acquisition are provided elsewhere.[60]

XES was performed for the Fe on the same instrument with an industrial Pd tube source (VAREX) operated at 30 kV and 3 mA (90 W). The sample fluorescence was analyzed and refocused at the detector position through the 0.5 mm slit and Si(440) spherically bent crystal analyzers (SBCA). Absorption spectra were calculated according to the transmission relation $\mu(E) \approx \ln(I_0/I_t)$ using a python-based software (easyXAFS LLC), also used for the dead time correction and energy calibration). The reduced data were further processed and analyzed using the Larch software.[61] The $\chi(k)$ data were isolated by subtracting a smooth polynomial approximating the $\mu0(E)$ background. The k^3-weighted $\chi(k)$ data were Fourier transformed after applying a Hanning window function ($dk = 2$). The Fourier transformation of the Mn and Fe K-edges is considered to represent the effective radial distribution of near-neighbor distances. However, due to the significant noise ratio at high k region for the Co, Ni, and Cu K-edges, their Fourier transformations are considered less informative.

TGA (TA Instruments Q5000) was performed at a heating rate of 5 °C min^{-1} under ambient air.

The sample morphology was characterized by means of TEM. High-angle annular dark-field scanning TEM (HAADF STEM) was conducted at 300 kV using a Thermo Fisher Themis Z equipped with a probe-corrector (S-CORR). Drift-corrected elemental mapping was done using an energy dispersive X-ray spectroscopy (EDS) detector (Thermo Fisher Super-X).

ICP-OES was performed on a SPECTRO ARCOS SOP instrument. For ICP-OES, the samples were dissolved in hydrochloric acid and diluted with deionized water.

XPS measurements were performed on a SPECS XPS system with PHOIBOS 150 energy analyzer using monochromatic Al K$_\alpha$ radiation (1486.6 eV), a take-off angle of 45° and pass energies at the electron analyzer of 30 (for detail scans) and 90 eV (for survey scans). The C1s peak of adventitious carbon at 284.8 eV was used for binding energy calibration.

Electrode Preparation: The HCF-based electrodes consisted of active material (70 wt%), Super C65 carbon black (TIMCAL, 20 wt%), and polyvinylidene difluoride binder (PVdF Solef 5130, Solvay, 10 wt%). PVdF was dissolved in N-methyl-2-pyrrolidone (Sigma-Aldrich) and then combined with Super C65 carbon black and active material using a Thinky ARE-250 mixer to form a viscous slurry. Next, the slurry was cast onto Al foil using a laboratory doctor blade (180 μm wet-film thickness). After drying in a vacuum at 120 °C for 24 h, 13 mm diameter circular electrodes were punched out and further dried for 12 h. The areal active material loading was in the range of 1.8–2.4 mg cm^{-2}.

Electrochemical Testing: The cycling performance was evaluated either in CR2032 coin cells or in Swagelok-type three-electrode cells using Na metal as counter and reference electrode. All cells were assembled in an Ar glovebox (MBraun UNIlab, [H_2O] and [O_2] < 0.1 ppm). The electrolyte consisted of 1 M $NaClO_4$ in ethylene carbonate/dimethyl carbonate/propylene carbonate (EC:DMC:PC, 1:1:1 by volume) with 5% fluoroethylene carbonate. Prior to electrochemical characterization, the cells were allowed to rest for 5 h. CV was carried out in a voltage range of 2.0–4.1 V versus Na$^+$/Na using a VMP3 potentiostat (BioLogic). Galvanostatic cycling tests were performed on two types of battery testers (MACCOR, Model 4300 and Landt CT3001A) with lower and upper cut-off voltages of 2.0 and 4.1 V versus Na$^+$/Na. All measurements were done in climatic chambers with a set temperature of 25 (±1) °C.

Operando XRD Analysis: XRD measurements were conducted on customized coin cells with Kapton windows of diameter 4 mm. The electrodes used had a higher areal active material loading of 6 mg cm^{-2}. Galvanostatic cycling was done at a specific current of 7 mA g^{-1} in the same voltage range using a SP-150 potentiostat/galvanostat (BioLogic). Patterns were collected using a STOE Stadi P diffractometer equipped with a Ga-jet X-ray source (Ga K$_\beta$ radiation, $\lambda = 1.20793$ Å).

Ex-Situ XRD Analysis: XRD was performed using the same coin cell setup as for the operando XRD measurements. Patterns were collected

**ADVANCED
SCIENCE NEWS**

www.advancedsciencenews.com

**ADVANCED
FUNCTIONAL
MATERIALS**

www.afm-journal.de

using a STOE Stadi P diffractometer with a Mo anode ($\lambda = 0.70926$ Å) and a DECTRIS MYTHEN 1K strip detector in transmission geometry.

DFT Simulations: All calculations were done using VASP6.2.[62] The linearized augmented-plane-wave (LAPW) method was applied to describe the electron wave functions with an energy cut-off of 520 eV and pseudopotentials for all atoms (PBE5.4). Gamma point geometry optimization was done until the maximum force on each individual atom was 0.01 eV Å^{-1} and the delta energy between self-consistent field (SCF) cycles was less than 10^{-6} eV.

Statistical Analysis: Electrochemical testing was done on at least three individual cells per HCF material. The data were analyzed by (one-sample) Student's *t*-test using OriginPro 2021 from OriginLab Corp.

Supporting Information

Supporting Information is available from the Wiley Online Library or from the author.

Conflict of Interest

The authors declare no conflict of interest.

Data Availability Statement

The data that support the findings of this study are available from the corresponding author upon reasonable request.

[1] Y. Ma, Y. Ma, Q. Wang, S. Schweidler, M. Botros, T. Fu, H. Hahn, T. Brezesinski, B. Breitung, *Energy Environ. Sci.* **2021**, *14*, 2883.

[2] C. Oses, C. Toher, S. Curtarolo, *Nat. Rev. Mater.* **2020**, *5*, 295.

[3] A. Amiri, R. Shahbazian-Yassar, *J. Mater. Chem. A* **2021**, *9*, 782.

[4] Q. Wang, L. Velasco, B. Breitung, V. Presser, *Adv. Energy Mater.* **2021**, *11*, 2102355.

[5] E. P. George, D. Raabe, R. O. Ritchie, *Nat. Rev. Mater.* **2019**, *4*, 515.

[6] M. C. Gao, D. B. Miracle, D. Maurice, X. Yan, Y. Zhang, J. A. Hawk, *J. Mater. Res.* **2018**, *33*, 3138.

[7] A. Sarkar, Q. Wang, A. Schiele, M. R. Chellali, S. S. Bhattacharya, D. Wang, T. Brezesinski, H. Hahn, L. Velasco, B. Breitung, *Adv. Mater.* **2019**, *31*, 1806236.

[8] Y. Zheng, Y. Yi, M. Fan, H. Liu, X. Li, R. Zhang, M. Li, Z. A. Qiao, *Energy Storage Mater.* **2019**, *23*, 678.

[9] J. Yan, D. Wang, X. Zhang, J. Li, Q. Du, X. Liu, J. Zhang, X. Qi, *J. Mater. Sci.* **2020**, *55*, 6942.

[10] Z. Lun, B. Ouyang, D.-H. Kwon, Y. Ha, E. E. Foley, T.-Y. Huang, Z. Cai, H. Kim, M. Balasubramanian, Y. Sun, J. Huang, Y. Tian, H. Kim, B. D. McCloskey, W. Yang, R. J. Clément, H. Ji, G. Ceder, *Nat. Mater.* **2021**, *20*, 214.

[11] B. Breitung, Q. Wang, A. Schiele, Ð. Tripković, A. Sarkar, L. Velasco, D. Wang, S. S. Bhattacharya, H. Hahn, T. Brezesinski, *Batteries Supercaps* **2020**, *3*, 361.

[12] Q. Wang, A. Sarkar, Z. Li, Y. Lu, L. Velasco, S. S. Bhattacharya, T. Brezesinski, H. Hahn, B. Breitung, *Electrochem. Commun.* **2019**, *100*, 121.

[13] A. Sarkar, L. Velasco, D. Wang, Q. Wang, G. Talasila, L. de Biasi, C. Kübel, T. Brezesinski, S. S. Bhattacharya, H. Hahn, B. Breitung, *Nat. Commun.* **2018**, *9*, 3400.

[14] Q. Wang, A. Sarkar, D. Wang, L. Velasco, R. Azmi, S. S. Bhattacharya, T. Bergfeldt, A. Düvel, P. Heitjans, T. Brezesinski, H. Hahn, B. Breitung, *Energy Environ. Sci.* **2019**, *12*, 2433.

[15] C. Zhao, F. Ding, Y. Lu, L. Chen, Y. Hu, *Angew. Chem., Int. Ed.* **2020**, *59*, 264.

[16] J. Wang, D. Stenzel, R. Azmi, S. Najib, K. Wang, J. Jeong, A. Sarkar, Q. Wang, P. A. Sukkurji, T. Bergfeldt, M. Botros, J. Maibach, H. Hahn, T. Brezesinski, B. Breitung, *Electrochem* **2020**, *1*, 60.

[17] N. Qiu, H. Chen, Z. Yang, S. Sun, Y. Wang, Y. Cui, *J. Alloys Compd.* **2019**, *777*, 767.

[18] J. Wang, Y. Cui, Q. Wang, K. Wang, X. Huang, D. Stenzel, A. Sarkar, R. Azmi, T. Bergfeldt, S. S. Bhattacharya, R. Kruk, H. Hahn, S. Schweidler, T. Brezesinski, B. Breitung, *Sci. Rep.* **2020**, *10*, 18430.

[19] Y. Ma, Y. Ma, S. L. Dreyer, Q. Wang, K. Wang, D. Goonetilleke, A. Omar, D. Mikhailova, H. Hahn, B. Breitung, T. Brezesinski, *Adv. Mater.* **2021**, *33*, 2101342.

[20] Y. Tang, W. Li, P. Feng, M. Zhou, K. Wang, Y. Wang, K. Zaghib, K. Jiang, *Adv. Funct. Mater.* **2020**, *30*, 1908754.

[21] L. Wang, Y. Lu, J. Liu, M. Xu, J. Cheng, D. Zhang, J. B. Goodenough, *Angew. Chem., Int. Ed.* **2013**, *52*, 1964.

[22] W. Li, C. Han, W. Wang, Q. Xia, S. Chou, Q. Gu, B. Johannessen, H. Liu, S. Dou, *Adv. Energy Mater.* **2020**, *10*, 1903006.

[23] Y. Shang, X. Li, J. Song, S. Huang, Z. Yang, Z. J. Xu, H. Y. Yang, *Chem* **2020**, *6*, 1804.

[24] J. Song, L. Wang, Y. Lu, J. Liu, B. Guo, P. Xiao, J. J. Lee, X. Q. Yang, G. Henkelman, J. B. Goodenough, *J. Am. Chem. Soc.* **2015**, *137*, 2658.

[25] L. Jiang, Y. Lu, C. Zhao, L. Liu, J. Zhang, Q. Zhang, X. Shen, J. Zhao, X. Yu, H. Li, X. Huang, L. Chen, Y. S. Hu, *Nat. Energy* **2019**, *4*, 495.

[26] J. C. Pramudita, S. Schmid, T. Godfrey, T. Whittle, M. Alam, T. Hanley, H. E. A. Brand, N. Sharma, *Phys. Chem. Chem. Phys.* **2014**, *16*, 24178.

[27] M. Giorgetti, M. Berrettoni, *Inorg. Chem.* **2008**, *47*, 6001.

[28] D. Wardecki, D. O. Ojwang, J. Grins, G. Svensson, *Cryst. Growth Des.* **2017**, *17*, 1285.

[29] H. He, X. Zeng, H. Wang, N. Chen, D. Sun, Y. Tang, X. Huang, Y. Pan, *J. Electrochem. Soc.* **2015**, *162*, A39.

**ADVANCED
SCIENCE NEWS**

www.advancedsciencenews.com

**ADVANCED
FUNCTIONAL
MATERIALS**

www.afm-journal.de

[30] I. Sarhid, I. Lampre, D. Dragoe, P. Beaunier, B. Palpant, H. Remita, *Materials* **2019**, *12*, 3012.

[31] Y. Huang, M. Xie, J. Zhang, Z. Wang, Y. Jiang, G. Xiao, S. Li, L. Li, F. Wu, R. Chen, *Nano Energy* **2017**, *39*, 273.

[32] Y. Liu, D. He, R. Han, G. Wei, Y. Qiao, *Chem. Commun.* **2017**, *53*, 5569.

[33] J. Li, L. He, J. Jiang, Z. Xu, M. Liu, X. Liu, H. Tong, Z. Liu, D. Qian, *Electrochim. Acta* **2020**, *353*, 136579.

[34] Y. Ma, Y. Ma, G. Giuli, T. Diemant, R. J. Behm, D. Geiger, U. Kaiser, U. Ulissi, S. Passerini, D. Bresser, *Sustainable Energy Fuels* **2018**, *2*, 2601.

[35] M. C. Biesinger, B. P. Payne, A. P. Grosvenor, L. W. M. Lau, A. R. Gerson, R. St, C. Smart, *Appl. Surf. Sci.* **2011**, *257*, 2717.

[36] X. Zhang, M. Xia, T. Liu, N. Peng, H. Yu, R. Zheng, L. Zhang, M. Shui, J. Shu, *Chem. Eng. J.* **2021**, *421*, 127767.

[37] M. Giorgetti, S. Della Longa, M. Benfatto, *J. Phys. Conf. Ser.* **2009**, *190*, 012145.

[38] M. Giorgetti, L. Guadagnini, D. Tonelli, M. Minicucci, G. Aquilanti, *Phys. Chem. Chem. Phys.* **2012**, *14*, 5527.

[39] C. A. Chatzidimitriou-Dreismann, T. Abdul-Redah, B. Kolaric, I. Juranic, *Phys. Rev. Lett.* **2000**, *84*, 5237.

[40] J. Sottmann, F. L. M. Bernal, K. V. Yusenko, M. Herrmann, H. Emerich, D. S. Wragg, S. Margadonna, *Electrochim. Acta* **2016**, *200*, 305.

[41] Y. Moritomo, M. Takachi, Y. Kurihara, T. Matsuda, *Adv. Mater. Sci. Eng.* **2013**, *2013*, 967285.

[42] T. E. Westre, P. Kennepohl, J. G. DeWitt, B. Hedman, K. O. Hodgson, E. I. Solomon, *J. Am. Chem. Soc.* **1997**, *119*, 6297.

[43] S. Lafuerza, A. Carlantuono, M. Retegan, P. Glatzel, *Inorg. Chem.* **2020**, *59*, 12518.

[44] C. J. Pollock, M. U. Delgado-Jaime, M. Atanasov, F. Neese, S. Debeer, *J. Am. Chem. Soc.* **2014**, *136*, 9453.

[45] J. Qian, C. Wu, Y. Cao, Z. Ma, Y. Huang, X. Ai, H. Yang, *Adv. Energy Mater.* **2018**, *8*, 1702619.

[46] Y. Ma, Y. Ma, H. Euchner, X. Liu, H. Zhang, B. Qin, D. Geiger, J. Biskupek, A. Carlsson, U. Kaiser, A. Groß, S. Indris, S. Passerini, D. Bresser, *ACS Energy Lett.* **2021**, *6*, 915.

[47] Y. Ma, Y. Ma, G. Giuli, H. Euchner, A. Groß, G. O. Lepore, F. D'Acapito, D. Geiger, J. Biskupek, U. Kaiser, H. M. Schütz, A. Carlsson, T. Diemant, R. J. Behm, M. Kuenzel, S. Passerini, D. Bresser, *Adv. Energy Mater.* **2020**, *10*, 2000783.

[48] Z. Wang, Y. Huang, R. Luo, F. Wu, L. Li, M. Xie, J. Huang, R. Chen, *J. Power Sources* **2019**, *436*, 226868.

[49] W. J. Li, S. L. Chou, J. Z. Wang, Y. M. Kang, J. L. Wang, Y. Liu, Q. F. Gu, H. K. Liu, S. X. Dou, *Chem. Mater.* **2015**, *27*, 1997.

[50] W. Ren, M. Qin, Z. Zhu, M. Yan, Q. Li, L. Zhang, D. Liu, L. Mai, *Nano Lett.* **2017**, *17*, 4713.

[51] J. Peng, J. Wang, H. Yi, W. Hu, Y. Yu, J. Yin, Y. Shen, Y. Liu, J. Luo, Y. Xu, P. Wei, Y. Li, Y. Jin, Y. Ding, L. Miao, J. Jiang, J. Han, Y. Huang, *Adv. Energy Mater.* **2018**, *8*, 1702856.

[52] X. Bie, K. Kubota, T. Hosaka, K. Chihara, S. Komaba, *J. Power Sources* **2018**, *378*, 322.

[53] L. Li, P. Nie, Y. Chen, J. Wang, *J. Mater. Chem. A* **2019**, *7*, 12134.

[54] W. Li, F. Zhang, X. Xiang, X. Zhang, *J. Phys. Chem. C* **2017**, *121*, 27805.

[55] Y. Lu, L. Wang, J. Cheng, J. B. Goodenough, *Chem. Commun.* **2012**, *48*, 6544.

[56] C. H. Li, M. K. Peprah, D. Asakura, M. W. Meisel, M. Okubo, D. R. Talham, *Chem. Mater.* **2015**, *27*, 1524.

[57] H. Fu, C. Liu, C. Zhang, W. Ma, K. Wang, Z. Li, X. Lu, G. Cao, *J. Mater. Chem. A* **2017**, *5*, 9604.

[58] E. P. Jahrman, W. M. Holden, A. S. Ditter, D. R. Mortensen, G. T. Seidler, T. T. Fister, S. A. Kozimor, L. F. J. Piper, J. Rana, N. C. Hyatt, M. C. Stennett, *Rev. Sci. Instrum.* **2019**, *90*, 024106.

[59] B. Ravel, M. Newville, *J. Synchrotron Radiat.* **2005**, *12*, 537.

[60] Y. S. Moghadam, A. El Kharbachi, T. Diemant, G. Melinte, Y. Hu, M. Fichtner, *Chem. Mater.* **2021**, *33*, 8235.

[61] M. Newville, *J. Phys. Conf. Ser.* **2013**, *430*, 012007.

[62] G. Kresse, J. Furthmu, *Phys. Rev. B* **1996**, *54*, 11169.